First-principles study of electron and hole mobilities of Si and GaAs

Jinlong Ma,[1,2] Arun S. Nissimagoudar,[1,2] and Wu Li[1,*]

[1]*Institute for Advanced Study, Shenzhen University, Shenzhen 518060, China*

[2]*Key Laboratory of Optoelectronic Devices and Systems of Ministry of Education and Guangdong Province, College of Optoelectronic Engineering, Shenzhen University, Shenzhen 518060, China*

(Received 1 August 2017; revised manuscript received 29 November 2017; published 4 January 2018)

With first-principles calculated electron-phonon coupling matrix elements, the phonon-limited electron and hole mobilities of Si and GaAs are studied using the Boltzmann transport equation. The calculated mobilities agree well with the experimental measurements. For electrons in GaAs, the calculated mobility is very sensitive to the band structure characterized by the effective mass and the energy gap between Γ and L valleys, which clarifies the discrepancies between recent literature findings [J.-J. Zhou and M. Bernardi, Phys. Rev. B **94**, 201201(R) (2016); T.-H. Liu *et al.*, Phys. Rev. B **95**, 075206 (2017)]. Unlike electrons in GaAs, where the longitudinal optical phonon dominates the scattering, the other phonon branches have a comparable influence on the mobility of holes in GaAs. In Si and GaAs, the spin-orbit coupling interaction has a significant effect on the valence bands and, further, on the hole mobilities, without which the calculated mobility is underestimated, especially at relatively low temperatures, while it has almost no effect on the electrons.

DOI: 10.1103/PhysRevB.97.045201

I. INTRODUCTION

With the advantage of being parameter-free and high accuracy, the first-principles calculation plays an increasingly important role in the discovery and development of functional materials. In the past decade, the first-principles investigation of phonon transport has been successfully applied to many systems, and several open-source packages exist nowadays [1–3]. In contrast, the first-principles calculation of electron transport in semiconductors is still in its infancy due to the challenge of electron-phonon coupling calculation [4]. Considering that only the carriers around the band edge are well excited and phonons have a much lower energy scale than electrons, very dense meshes of Brillouin zone (BZ) are needed for both electrons and phonons, especially for materials with a small effective electron mass. As a consequence, the first-principles calculation of electron-phonon coupling interaction is extremely time-consuming and beyond the current computational capacities. The method that approximates the electron-phonon coupling scattering with adjustable relaxation times by fitting experimental data loses the physical details and is not predictive. As many unprecedented materials are generated from modern technologies, a parameter-free calculation becomes badly needed.

The bottleneck of electron-phonon coupling calculation can be overcome by using the Wannier function interpolation method [5–7], in which the first-principles calculations need only be performed on coarse grids. This method has been employed in nonpolar materials such as Si and black phosphorene [8,9]. In polar materials, electrons interact strongly with longitudinal optical phonons due to the induced macroscopic polarization field, which causes the electron-phonon coupling matrix element to diverge with decreasing phonon wave vector [10]. Wannier function interpolation from relatively coarse grids can easily lose such long-range information. In the case of isotropic three-dimensional systems, the polar effect can be taken into account by applying the Fröhlich formula correction [11]. Later, Verdi *et al.* [6,7] and Sjakste *et al.* [12] proposed the general "polar Wannier function interpolation scheme," unifying the treatments of nonpolar and polar systems in a convenient calculational framework.

Si and GaAs are two of the most widely used semiconductors in electronic devices. In 2015, Qiu *et al.* [8] applied Wannier function interpolation to electron-phonon coupling matrix elements and studied the thermoelectric properties of *n*-type Si under the energy relaxation time approximation (ERTA) of the Boltzmann transport equation (BTE). Soon afterward, one of the authors of this work used linear interpolation and demonstrated an iterative solution of the BTE [13]. Li obtained more accurate phonon-limited scattering rates, implying the importance of accurate BZ integration of the δ function enabled by a Gaussian smearing method with locally adaptive broadening parameters [13]. Very recently, Zhou *et al.* [14] and Liu *et al.* [15] applied polar Wannier function interpolation to GaAs. Zhou *et al.* obtained a room-temperature mobility of 8900 $cm^2\ V^{-1}\ s^{-1}$ under the ERTA for electrons in GaAs. However, the ERTA value obtained by Liu *et al.* is much smaller, only 7050 $cm^2\ V^{-1}\ s^{-1}$, and the iterative solution from the BTE gives 8340 $cm^2\ V^{-1}\ s^{-1}$.

In this study, the electron and hole mobilities of Si and GaAs are studied. The Wannier function interpolation method is used to obtain sufficient electron-phonon coupling elements and an iterative scheme is performed for solving the BTE. We find that the ERTA of the BTE is reliable for Si due to the very small difference compared to the exact solution. However, the ERTA strongly underestimates the mobility of GaAs, suggesting that the iterative solution of the BTE for GaAs is necessary.

*wu.li.phys2011@gmail.com

Differently from the ERTA, the momentum relaxation time approximation (MRTA) gives a good agreement with the exact values for both Si and GaAs. Additionally, the electron mean free path (MFP) is analyzed, which is found to be much smaller than the corresponding phonon transport, with the MFPs below a few hundreds of nanometers for electrons and below a few tens of nanometers for holes at room temperature.

II. METHODOLOGY

In the presence of an external electric field $\mathbf{E}$, the electron distribution function $f_{n\mathbf{k}}$ of the $n\mathbf{k}$ state deviates from its equilibrium Fermi-Dirac distribution $f^0_{n\mathbf{k}}$. Due to internal phonon scattering mechanisms, the system can reach a steady state. In the steady state, the deviated $f_{n\mathbf{k}}$ can be obtained from the BTE as [13]

$$-\frac{q\mathbf{E}}{\hbar}\frac{\partial f_{n\mathbf{k}}}{\partial \mathbf{k}} + \left.\frac{\partial f_{n\mathbf{k}}}{\partial t}\right|_{\text{scatt}} = 0, \tag{1}$$

where q is the elementary charge and $\hbar$ is the reduced Plank constant. For a weak electric field, the BTE can be linearized with $f_{n\mathbf{k}} = f^0_{n\mathbf{k}} + f^0_{n\mathbf{k}}(1 - f^0_{n\mathbf{k}})\Phi_{n\mathbf{k}}$, with $\Phi_{n\mathbf{k}}$ being a small perturbation. Since $\Phi_{n\mathbf{k}}$ is linear with $\mathbf{E}$, it is convenient to write $\Phi_{n\mathbf{k}} = \frac{q\mathbf{E}}{k_B T}\cdot\mathbf{F}_{n\mathbf{k}}$, where k_B is the Boltzmann constant, T is the temperature, and $\mathbf{F}_{n\mathbf{k}}$ can be regarded as the mean free displacement [1,13]. When only electron-phonon scattering is considered, the linearized BTE can be written as [13]

$$\mathbf{F}_{n\mathbf{k}} = \mathbf{v}_{n\mathbf{k}}\tau^0_{n\mathbf{k}} + \tau^0_{n\mathbf{k}}\sum_{\mathbf{q}pm}\left(\Gamma^{m\mathbf{k}+\mathbf{q}}_{n\mathbf{k},\mathbf{q}p} + \Gamma^{m\mathbf{k}+\mathbf{q},-\mathbf{q}p}_{n\mathbf{k}}\right)\mathbf{F}_{m\mathbf{k}+\mathbf{q}}, \tag{2}$$

where $\mathbf{v}_{n\mathbf{k}}$ is the electron group velocity, and $\mathbf{q}p$ denotes the phonon mode. $\Gamma^{m\mathbf{k}+\mathbf{q}}_{n\mathbf{k},\mathbf{q}p}$ and $\Gamma^{m\mathbf{k}+\mathbf{q},-\mathbf{q}p}_{n\mathbf{k}}$ are transition rates, which can be determined from the first-principles-calculated electron-phonon coupling strength, for phonon absorption and emission processes, respectively [13]. For convenience, $\Gamma^{m\mathbf{k}+\mathbf{q}}_{n\mathbf{k},\mathbf{q}p}$ and $\Gamma^{m\mathbf{k}+\mathbf{q},-\mathbf{q}p}_{n\mathbf{k}}$ here differ by a factor of $f^0_{n\mathbf{k}}(1 - f^0_{n\mathbf{k}})$ from those in Ref. [13]. $\tau^0_{n\mathbf{k}} = [\sum_{\mathbf{q}pm}(\Gamma^{m\mathbf{k}+\mathbf{q}}_{n\mathbf{k},\mathbf{q}p} + \Gamma^{m\mathbf{k}+\mathbf{q},-\mathbf{q}p}_{n\mathbf{k}})]^{-1}$ is the relaxation time.

The exact $\mathbf{F}_{n\mathbf{k}}$ can be obtained by performing the iterative solution of Eq. (2). This iterative scheme for solving the linearized BTE has been applied intensively to phonon transport [1,16,17] and, recently, to electron transport [13,15]. The $\mathbf{k}$ and $\mathbf{q}$ grids need to be commensurate [5,6]. If the sum term on the right side is neglected, the solution is called the ERTA. Another widely used approximation is the MRTA, which is similar to the ERTA but additionally considers the relative change of the electron velocity in each scattering process by multiplying the terms $\Gamma^{m\mathbf{k}+\mathbf{q}}_{n\mathbf{k},\mathbf{q}p}$ and $\Gamma^{m\mathbf{k}+\mathbf{q},-\mathbf{q}p}_{n\mathbf{k}}$ with an efficiency factor of [13]

$$\lambda = 1 - \frac{\mathbf{v}_{m\mathbf{k}+\mathbf{q}}\cdot\mathbf{v}_{n\mathbf{k}}}{|\mathbf{v}_{n\mathbf{k}}|^2}. \tag{3}$$

Once $\mathbf{F}_{n\mathbf{k}}$ is obtained, the electric conductivity tensor can be formulated with

$$\sigma^{\alpha\beta} = \frac{2q^2}{NVk_BT}\sum_{n\mathbf{k}} f^0_{n\mathbf{k}}\left(1 - f^0_{n\mathbf{k}}\right)v^\alpha_{n\mathbf{k}}F^\beta_{n\mathbf{k}}, \tag{4}$$

where N is the number of $\mathbf{k}$ meshes, V is the volume of the unit cell, α and β is the Cartesian direction. Finally, the mobility is calculated as

$$\mu^{\alpha\beta} = \frac{\sigma^{\alpha\beta}}{n_c q}, \tag{5}$$

where n_c is the carrier density. In the n-type case, $n_c = \frac{2}{NV}\sum_{n\mathbf{k}} f^0_{n\mathbf{k}}$, while in the p-type case, $n_c = \frac{2}{NV}\sum_{n\mathbf{k}}(1 - f^0_{n\mathbf{k}})$.

III. RESULTS AND DISCUSSION

The electronic band structure, phonon dispersion, and initial electron-phonon coupling matrix were calculated from density functional theory (DFT) and density functional perturbation theory using the QUANTUM ESPRESSO package [18] with norm-conserving pseudopotential under the local density approximation [19,20]. The spin-orbit coupling (SOC) interaction was considered in the calculation. The cutoff energy of plane waves was set to be 48 Ry, and $16 \times 16 \times 16$ Monkhorst-Pack $\mathbf{k}$ meshes were used for structure relaxation. The relaxed lattice constants for Si and GaAs are 5.39 and 5.55 Å, respectively, in good agreement with experimental values [21,22]. The EPW package [6] was used to perform Wannier function interpolation for the electron-phonon coupling matrix. Initial coarse $6 \times 6 \times 6$ $\mathbf{k}$ and $6 \times 6 \times 6$ $\mathbf{q}$ meshes were used for both Si and GaAs [8,15]. The chemical potential was manually fixed to be 0.3 eV in the band gap away from the band edges, which is high enough to ensure that the calculated mobility is intrinsically phonon limited.

A. Si

Figure 1(a) shows the calculated electronic band structure of Si with and without SOC interaction. It can be seen that the SOC has almost no effect on the conduction bands, while it removes the triple degeneracy at the top of valence bands [23],

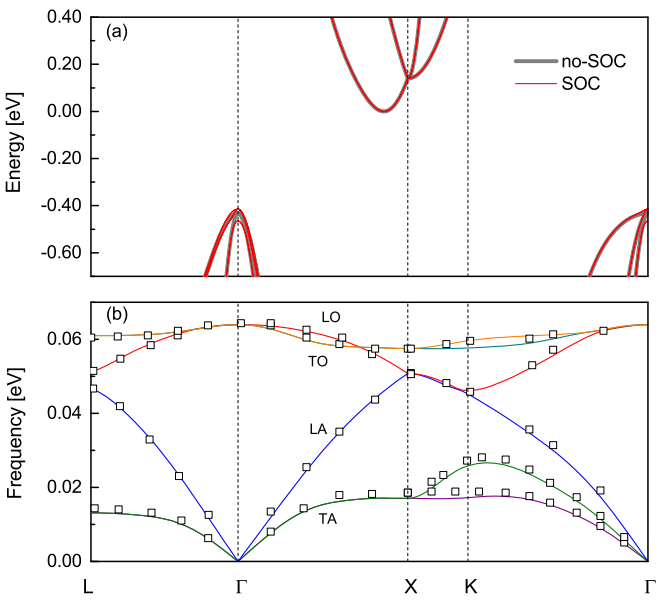

FIG. 1. (a) Electronic band structure of Si calculated with and without spin-orbit coupling interaction. (b) Phonon dispersion of Si along high-symmetry directions compared to the experimental data from Ref. [29].

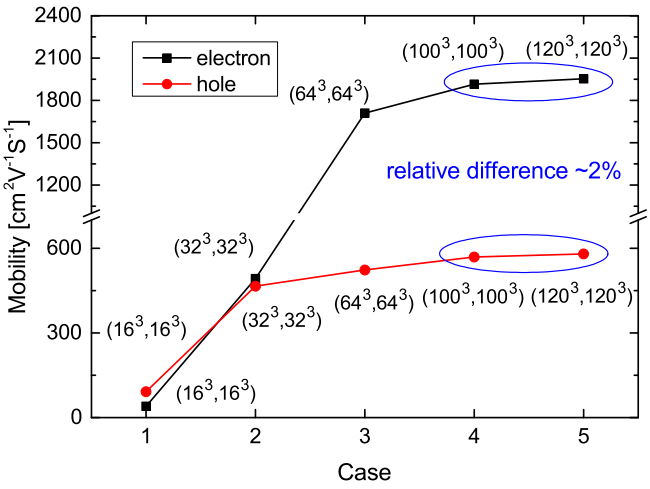

FIG. 2. Calculated mobilities of Si with respect to different (**k**,**q**) grids at room temperature.

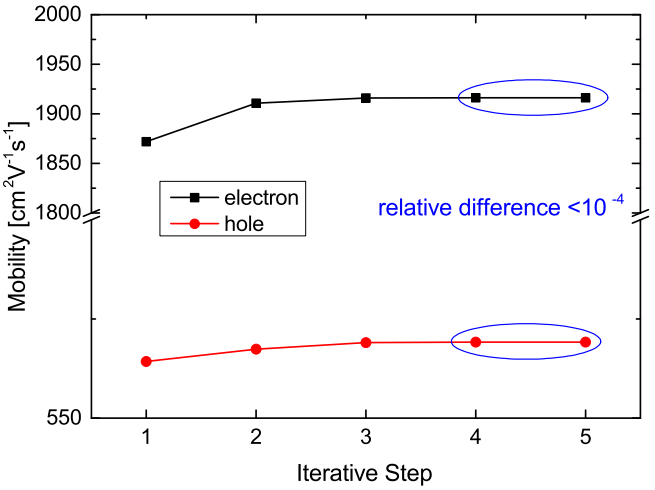

FIG. 3. Calculated mobilities of Si with respect to the iterative step at room temperature.

resulting in the small split-off energy gap of 0.05 eV, agreeing well with the experimental value of 0.044 eV [24]. The calculated band gap is about 0.42 eV, smaller than the experimental measurement [23–25], which is a known drawback of DFT. The effective masses at the band edges are calculated, as listed in Table I, and show good agreement with the experiments and other calculations [24,26–28]. Figure 1(b) shows the calculated phonon dispersion compared with the experimental results. The transverse acoustic (TA), longitudinal acoustic (LA), transverse optical (TO), and longitudinal optical (LO) branches are represented by different colors. It is clear that the phonon energy scale is very small compared to that of electrons.

In calculating the mobility, very dense **k** and **q** meshes are needed. The convergence of **k** and **q** meshes was checked. Figure 2 shows that the calculated mobilities of Si are converged with 120 × 120 × 120 **k** and **q** final grids. The locally adaptive broadening parameters depending on the specific scattering processes and the **q** grid size are employed for the Gaussian function approximation of delta functions [13]. In the iterative process, the convergence criterion is chosen to be 10^{-4}, i.e., to allow a relative difference of the mobilities in two successive steps. The mobilities with respect to iterative step are plotted in Fig. 3.

Figure 4 shows the calculated electron mobilities of Si, which are in good agreement with the experimental values in a wide temperature range [30–33]. The larger discrepancy at lower temperatures can be understood, since other scattering mechanisms beyond phonon scattering become more important in the experimental samples at lower temperatures, which are, however, not considered in the calculation. The calculated room-temperature mobility is about 1915 $cm^2\,V^{-1}\,s^{-1}$, which is slightly larger than the values of 1860 $cm^2\,V^{-1}\,s^{-1}$ reported in Ref. [13] and 1750 $cm^2\,V^{-1}\,s^{-1}$ reported in Ref. [34]. The difference is probably related to the interpolation of electron-phonon coupling matrix elements. Specifically, Ref. [13] directly uses linear interpolation from coarse grids to fine grids, and Ref. [34] uses Wannier function interpolation from coarse grids to relatively dense grids and then selects the value of the closest point for the final fine grids. In our calculation, the electron-phonon coupling matrix was accurately interpolated to very fine grids. The ERTA results are also plotted for comparison, which demonstrate a small discrepancy with the exact solution, agreeing with previous findings [13]. For instance, the room-temperature ERTA value is about 1872 $cm^2\,V^{-1}\,s^{-1}$, with an underestimation of only about 3%. The MRTA gives almost-identical values to the exact solution in the temperature range from 100 to 500 K, indicating improved correction to the ERTA in Si. The mobilities without considering the SOC interaction are also calculated, which are almost the same and thus not plotted here.

Figure 5 shows the calculated hole mobilities of Si at different temperatures. The calculations are in reasonable agreement with experimental values, with a calculated mobility of about 569 $cm^2\,V^{-1}\,s^{-1}$ at room temperature. The difference between ERTA and exact results is also very slight, smaller

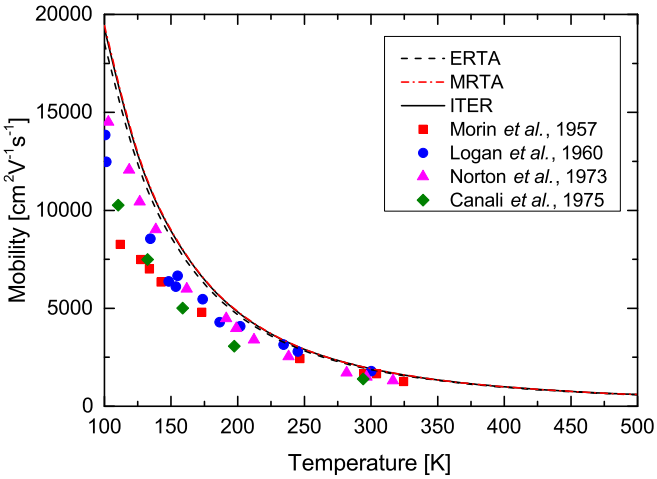

FIG. 4. Electron mobilities of Si calculated with the ERTA (dashed line), MRTA (dash-dotted line), and iterative solution (solid line) of the BTE. Symbols represent experimental measurements, with squares from Ref. [30], circles from Ref. [31], triangles from Ref. [32], and diamonds from Ref. [33].

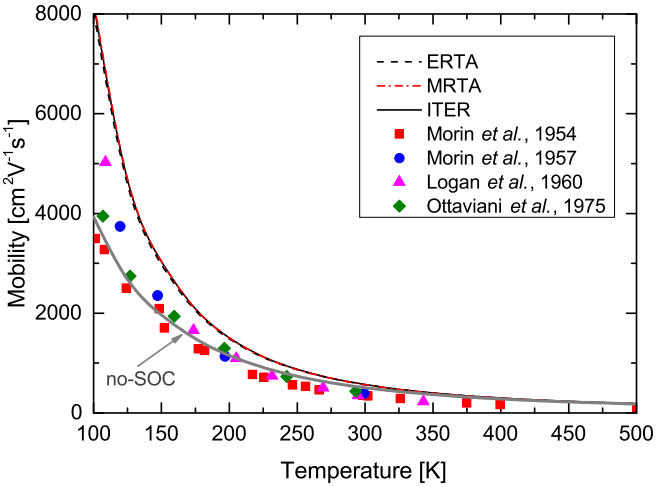

FIG. 5. Hole mobilities of Si calculated with the ERTA (dashed line), MRTA (dash-dotted line), and iterative solution (solid line) of the BTE. Symbols are experimental measurements, with squares from Ref. [35], circles from Ref. [30], triangles from Ref. [31], and diamonds from Ref. [36].

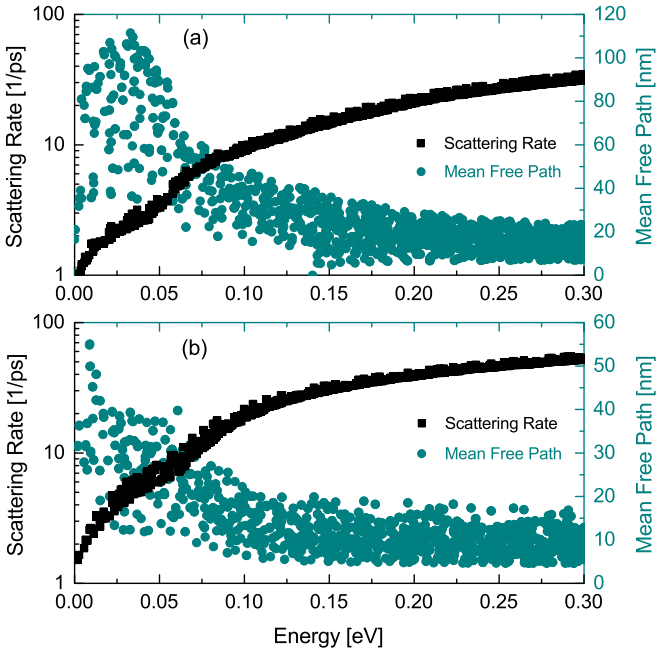

FIG. 6. Scattering rates and corresponding mean free paths of (a) electrons vs energy above the CBM and (b) holes vs energy below the VBM in Si at room temperature.

than 3% between 100 and 500 K. The MRTA again gives improved results compared to the ERTA, especially at lower temperatures. Therefore, the MRTA can be a very efficient approximation considering that the iterative solution can be very time-consuming in some algorithms where Wannier function interpolation needs to be performed at every single iteration step for the sake of saving memory usage. Note that previously a $16 \times 16 \times 16$ initial grid was required both for electrons and for phonons to get converged results within the linear interpolation method [13]. With Wannier function interpolation, only a $6 \times 6 \times 6$ grid is needed. Significant computational resources are thus saved. The iterative results of the BTE without the SOC effect are also plotted. The mobilities without SOC are obviously underestimated compared to the mobilities with SOC, especially at low temperatures. This is easily understood that the occurrence of band splitting has a stronger effect on low-energy electrons which make more relative contributions at low temperatures.

To understand the nanostructuring effect on the electron transport, it is useful to analyze the mode-specific contributions. Figures 6(a) and 6(b) show the room-temperature scattering rates vs the energy for electrons and holes of Si, respectively. It can be seen that a faster increase in scattering rates occurs around the energy of about 60 meV due to the occurrence of optical phonon emission processes, which has been revealed previously with dense BZ sampling enabled by linear interpolation [13]. The corresponding MFPs are also plotted, and they are less concentrated than the scattering rates. The MFP is defined as $\Lambda_{n\mathbf{k}} = |v_{n\mathbf{k}}| \cdot \tau^0_{n\mathbf{k}}$. So the enhanced difference in the MFP at a given energy should be due to the anisotropy of velocity close to the band edge, as revealed by the anisotropy of the electron effective mass in Table I. The largest electron MFP is 110 nm, corresponding to the energy of 33 meV above the conduction band minimum (CBM). After summing up the contribution from states with different energies, we found that the energy below 0.1 eV contributes about 95% to the mobility, which corresponds to the MFPs from 15 to 110 nm at room temperature, consistent with previous calculations [37–39] and experiments [40]. A similar analysis has also been done for holes in Si, which shows that the dominant contribution also comes from the holes within 0.1 eV below the valence band maximum (VBM). The corresponding MFPs are between 5 and 55 nm at room temperature, as shown in Fig. 6(b). The electron/hole MFPs are distributed over a

TABLE I. Band gap (ΔE_g) and split-off energy gap ($\Delta E_{\rm so}$) of Si, in units of eV, and electron and hole effective masses at band edges of Si, in units of the electron mass m_0.

	ΔE_g	$\Delta E_{\rm so}$	m_e^l	m_e^t	$m_{hh}^{(100)}$	$m_{lh}^{(100)}$	$m_{hh}^{(110)}$	$m_{lh}^{(110)}$	$m_{hh}^{(111)}$	$m_{lh}^{(111)}$	$m_{\rm so}$
This work	0.42	0.050	0.91	0.18	0.26	0.17	0.48	0.14	0.54	0.13	0.20
Experiment											
[24]	1.17	0.044	0.92	0.19							0.23
[26]			0.98	0.19	0.46	0.17	0.53	0.16	0.56	0.16	
Calculation											
[27]			0.96	0.16	0.26	0.18	0.54	0.14	0.67	0.13	0.22
[28]			0.95	0.19	0.22	0.22	0.36	0.17	0.66	0.13	0.22

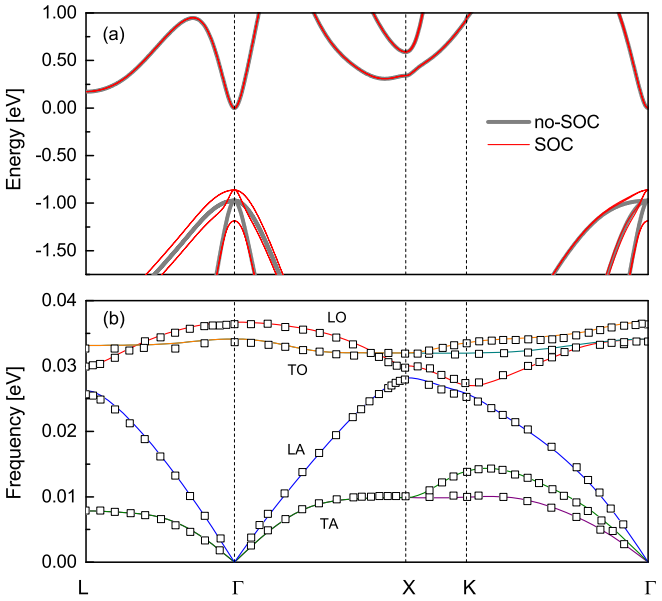

FIG. 7. (a) Electronic band structure of GaAs calculated with and without spin-orbit coupling interactions. (b) Phonon dispersion of GaAs along high-symmetry directions compared to experimental data from Ref. [50].

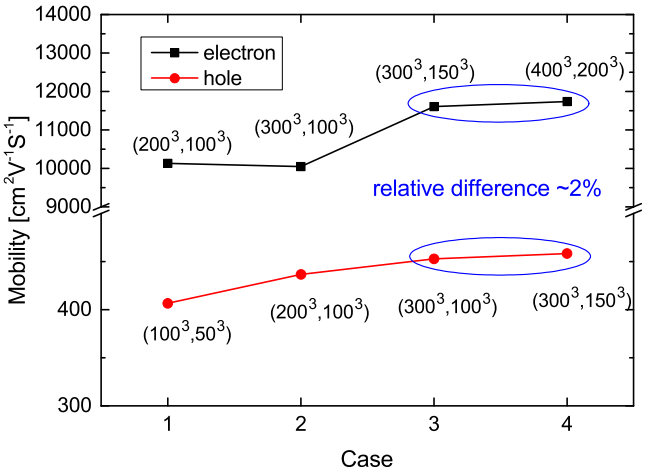

FIG. 8. Calculated mobilities of GaAs with respect to different (**k**,**q**) grids at room temperature.

narrow range and are much smaller than those of phonons, which generally span the large range from 10 nm to 10 μm in Si [41]. The fact that electrons have much smaller MFPs than phonons seems to hold for all materials. It indicates that nanostructuring can possibly reduce the thermal conductivity while leaving the electrical conductivity unchanged. This principle has been widely applied to thermoelectrical materials to improve the of merit (ZT) [8,42–44].

B. GaAs

Figure 7(a) shows the electronic band structure of GaAs with and without SOC interaction. SOC has a significant effect on the valence bands, resulting in a split-off energy gap of 0.33 eV, in good agreement with experiments and previous calculations [23,23,45]. The calculated direct bandgap, present at Γ, is about 0.86 eV, and the energy difference between the Γ and the L valleys is about 0.17 eV. Those values are smaller than the experimental measurements of about 1.52 and 0.22 eV, respectively [25]. The electron effective mass around Γ is very small and the calculated value of $0.050m_0$ is smaller than the experimental value of $0.066m_0$, while the hole effective mass is relatively large and in reasonable agreement with experiments and previous calculations [46–49], as listed in Table II. Figure 7(b) shows the calculated phonon dispersion, agreeing well with the experiments. The highest phonon frequency is about 35 meV.

Figure 8 shows the calculated mobilities of GaAs with respect to **k** and **q** grids. For electrons in GaAs, the $400 \times 400 \times 400$ **k** mesh almost ensures the convergence, in agreement with the finding in Ref. [14], where the mobility changes only about 1% when the **k** grids increase from 320^3 to 600^3, while the $200 \times 200 \times 200$ **q** mesh is sufficient for phonon. For holes, $300 \times 300 \times 300$ **k** mesh and $150 \times 150 \times 150$ **q** mesh are almost sufficient. The convergence criterion of the iterative BTE is also chosen to be 10^{-4}, as shown in Fig. 9.

Figure 10 shows the calculated electron mobilities of GaAs. At relatively low temperatures, the mobilities are much larger than the experimental values. In addition, we find a faster decrease above 350 K compared to the experiments and previous calculations [14,15]. This can be attributed to the fact that the calculated energy gap between the Γ and the L valleys is smaller than that in the experiments, which causes the scattering between the Γ and the L valleys to take effect at lower temperatures than it would actually. Unlike in Si, the ERTA significantly underestimates the solution, for instance, by almost 41% at room temperature. In the case of Si, the

TABLE II. Band gap (ΔE_g), split-off energy gap ($\Delta E_{\rm so}$), and Γ-L valley energy gap ($\Delta E_{\Gamma\rm L}$) of GaAs, in units of eV, and electron and hole effective masses of GaAs at band edges, in units of the electron mass m_0.

	ΔE_g	$\Delta E_{\rm so}$	$\Delta E_{\Gamma\rm L}$	m_e	$m_{hh}^{(100)}$	$m_{lh}^{(100)}$	$m_{hh}^{(110)}$	$m_{lh}^{(110)}$	$m_{hh}^{(111)}$	$m_{lh}^{(111)}$	$m_{\rm so}$
This work	0.86	0.33	0.17	0.050	0.31	0.059	0.48	0.055	0.59	0.054	0.13
Experiment											
[23]	1.52	0.34	0.22								
[46]				0.066	0.34	0.094			0.70		0.18
[47]					0.48	0.091			0.50	0.093	0.08
Calculation											
[48]				0.070	0.33	0.068			0.83	0.056	
[49]				0.030	0.32	0.036					0.11

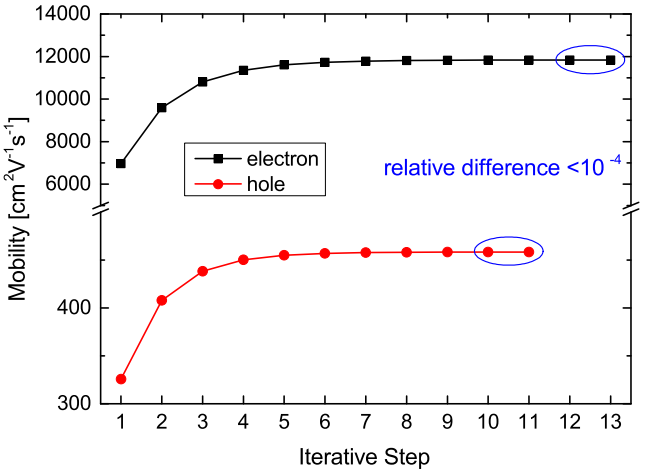

FIG. 9. Calculated mobilities of GaAs with respect to the iterative step at room temperature.

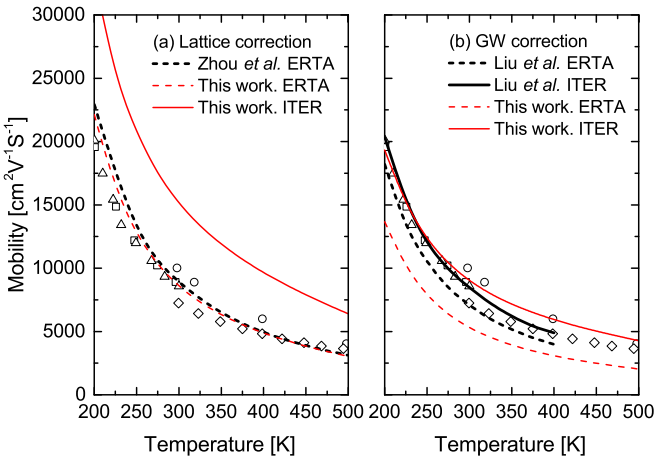

FIG. 11. Electron mobilities of GaAs calculated with (a) the lattice constant correction and (b) the GW correction, compared with Zhou *et al.* [14] and Liu *et al.* [15] as well as experiments (symbols).

phonon-caused scattering to electrons near the band edges are almost isotropic (intravalley scattering) or symmetric (intervalley scattering). As a consequence, the forward scattering is equal to the backward scattering, and the extra term in Eq. (2) is negligible [13,51].

In GaAs, the electron-phonon coupling elements of LO phonons are divergent around the Γ point due to polar interaction, and thus the scattering to different final electron states shows a strong directional dependence determined by the $|\mathbf{q}|$ involved. The forward scattering is no longer canceled out with the backward scattering, so the extra term in Eq. (2) cannot be neglected [15,51]. We have also examined the accuracy of the MRTA for GaAs, which is found to have better agreement with the exact solution than the ERTA does, with an overestimation of less than 30% between 200 and 500 K. As in Si, the calculation without SOC gives the same electron mobilities for GaAs.

It is noted that Refs. [14] and [15] show much better agreement with experiments than our calculation of the electron mobilities of GaAs. However, discrepancies still exist. The room-temperature ERTA result in Ref. [14] is 8900 cm^2 V^{-1} s^{-1}, which is much larger than the value of 7050 cm^2 V^{-1} s^{-1} reported in Ref. [15]. Moreover, Ref. [15] shows that the iterative solution of BTE gives 8340 cm^2 V^{-1} s^{-1}. In Ref. [14], the lattice constant was slightly increased, to 5.55 Å from its relaxed lattice constant of 5.53 Å, which gives an electron effective mass of $0.055m_0$ and Γ-L energy gap of 0.25 eV. Reference [15] applied the GW correction to the band structure. By using the same lattice constant and pseudopotential, we are able to reproduce the results in Ref. [14], as shown in Fig. 11(a). This demonstrates that our calculation does not suffer the singularity of long-range electron-phonon coupling and the $\mathbf{q}$ uniform sampling also works compared to the importance sampling method in Ref. [14]. The iterative

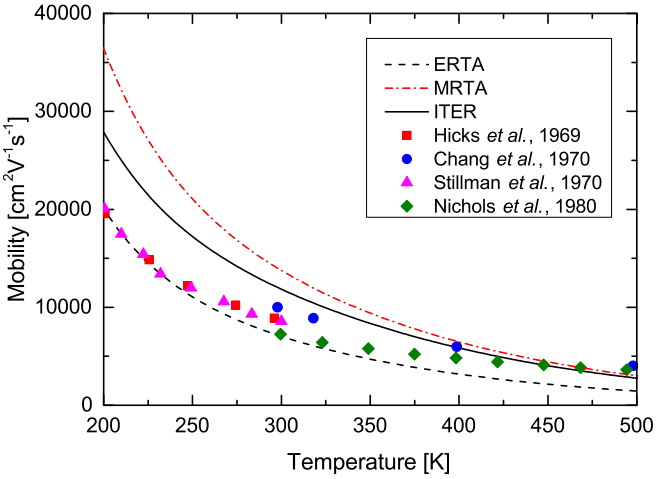

FIG. 10. Electron mobilities of GaAs calculated with the ERTA (dashed line), MRTA (dash-dotted line), and iterative solution (solid line) of the BTE. Symbols are experimental measurements, with squares from Ref. [52], circles from Ref. [53], triangles from Ref. [54], and diamonds from Ref. [55].

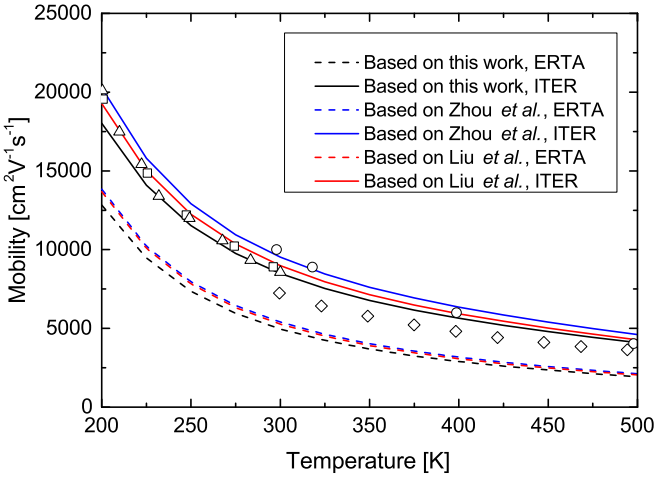

FIG. 12. Electron mobilities of GaAs calculated using the same GW-corrected conduction bands, while other related quantities are obtained from the raw calculation of this work, the lattice correction based on Zhou *et al.* [14], and the GW correction based on Liu *et al.* [15].

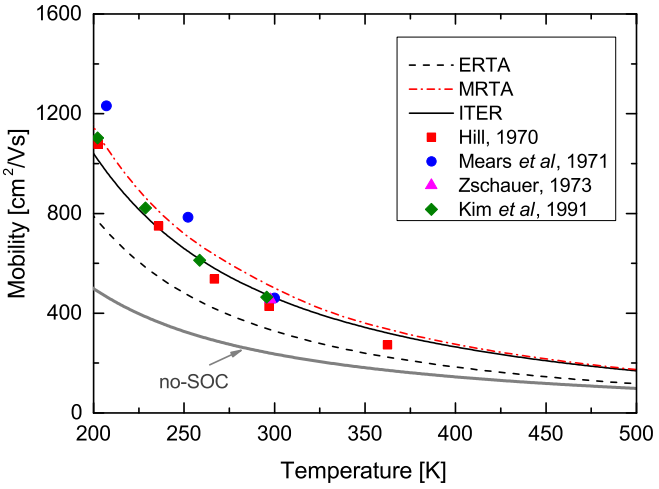

FIG. 13. Hole mobilities of GaAs calculated with the ERTA (dashed line), MRTA (dash-dotted line), and iterative solution (solid line) of the BTE. Symbols are experimental measurements, with squares from Ref. [56], circles from Ref. [57], triangles from Ref. [58], and diamonds from Ref. [59].

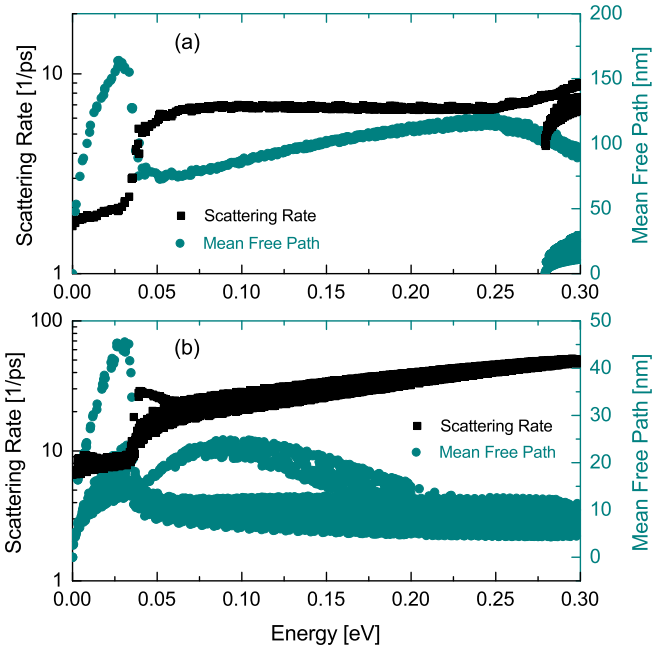

FIG. 14. Scattering rates and corresponding mean free paths of (a) electrons vs the energy above the CBM and (b) holes vs the energy below the VBM in GaAs at room temperature.

solution of the BTE under this condition is also given, which is much larger than the ERTA results. We also use the same pseudopotential and GW correction as in Ref. [15], however, as some calculational parameters are different, our calculation has some discrepancies with that in Ref. [15], as shown in Fig. 11(b). The ERTA solution is smaller than that in Ref. [15], while the iterative solution agrees with Ref. [15] at low temperatures but larger at relatively high temperatures, which still agrees reasonably with the experiments. The GW correction in the present calculation gives an electron effective mass of $0.061m_0$ and a Γ-L energy gap of 0.28 eV, which is larger than the 0.258 eV obtained in Ref. [15]. The calculated electron mobility is 8985 $cm^2\,V^{-1}\,s^{-1}$ at room temperature.

From the three cases above, distinguished as raw calculations in this work, lattice correction based on Ref. [14], and GW correction based on Ref. [15], the calculated mobility is very sensitive to the obtained band structure characterized by the effective mass and Γ-L energy gap. To see whether or not other factors such as the electron-phonon coupling matrix are also affected by the band structure and consequently change the mobility, we further manually employ the GW-corrected conduction bands used above in the raw calculation case and the lattice correction case, as the electron effective mass agrees better with experiments, while keeping the other related quantities such as phonon dispersion and electron-phonon coupling unchanged in each case. Figure 12 shows that the iterative solutions based on the raw case and lattice correction case are decreased compared to the original calculations. Both of them become close to the GW correction case and agree well with the experiments. The small difference between different cases suggest that the discrepancies between Ref. [14] and Ref. [15] mainly comes from the band structure, and not other factors like the electron-phonon coupling matrix.

Figure 13 shows the hole mobilities of GaAs under different solutions of the BTE. The iterative solution gives 459 $cm^2\,V^{-1}\,s^{-1}$ at room temperature, which is about 30% larger than the ERTA solution, with a value of 326 $cm^2\,V^{-1}\,s^{-1}$. The MRTA still has a much higher accuracy than the ERTA, and the difference between the MRTA and the exact result is about 10% at 200 K and becomes less at higher temperatures. For hole mobilities of GaAs, the SOC interaction has a strong effect. The mobility calculated without the SOC is much smaller than that with the SOC. For instance, the mobility without SOC is only about 235 $cm^2\,V^{-1}\,s^{-1}$ at room temperature, with an underestimation of 50%. As the temperature deceases, the underestimation increases.

It is also significant to have mode-specific analysis of the transport properties in GaAs. Figure 14(a) shows the scattering rates of electrons in GaAs with GW-corrected conduction bands at room temperature. In the calculation in Ref. [15], the scattering rates show a jump at 15 meV, which is attributed to the contribution of LA and TA phonon scatterings. However, the LA and TA scatterings obtained in Ref. [14] are smaller than the LO scattering by more than one order of magnitude. The calculated scattering rates in this work are more similar to those in Ref. [14], which show almost-constant scattering rates up to 35 meV due to the dominance of the LO phonon absorption process [15]. At 35 meV, the scattering rates show a more obvious jump, in agreement with Refs. [14] and [15], corresponding to the onset of LO phonon emission processes [13–15]. The mode-dependent MFPs are also plotted in Fig. 14(a), which shows clearly two separated parts. One part spans from 0 to 0.3 eV, illustrating electron states in the isotropic Γ valley. The other begins at 0.28 eV, representing electron states in the L valley, where the energy and scattering rates are anisotropic. The electron MFPs are in the range of 50–165 nm below 0.28 eV, agreeing with previous calculations [15] and experimental values [60,61].

The jump characteristic of scattering rates also exists for holes of GaAs, as shown in Fig. 14(b). Although there are different valence bands around Γ contributing to the transport,

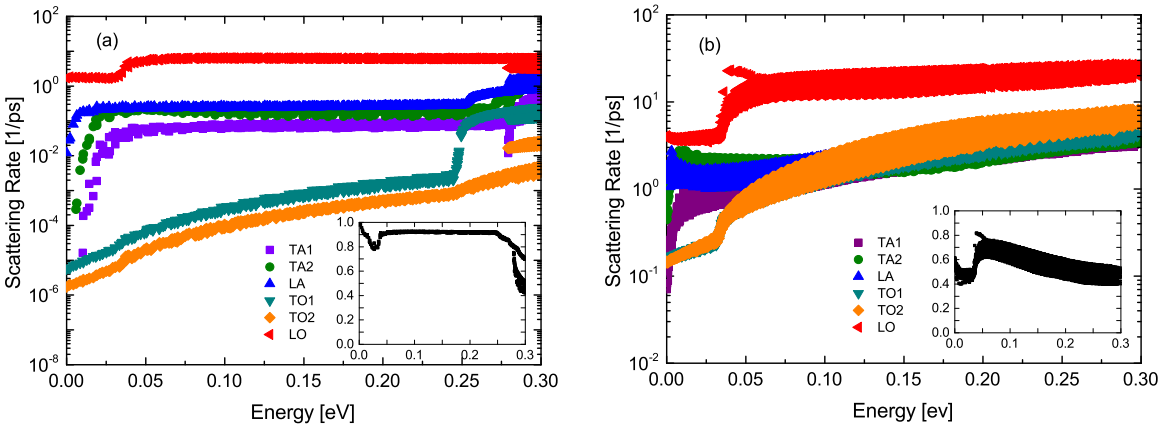

FIG. 15. Scattering rates of (a) electrons vs the energy above the CBM and (b) holes vs the energy below the VBM contributed by different phonon branches in GaAs at room temperature. Inset: Relative contribution from the LO branch.

the scattering rates show a weak band dependence. The MFPs of light holes are, however, larger than those of heavy holes due to the higher group velocity, as can be seen in Fig. 7. The largest MFP is 45 nm at room temperature, occurring around 35 meV. The MFPs of holes are much smaller than those of electrons, consistent with the fact that electrons have a much smaller mobility than holes in GaAs.

Figure 15(a) shows the scattering rates of electrons in GaAs contributed from different phonon branches at room temperature. They have a shape similar to that in Ref. [15], but with lower acoustic phonon scattering rates as reported by Zhou *et al.* in Ref. [14]. For electrons with an energy lower than 0.28 eV, the LO phonons contribute more than 80% to the total scattering, as shown in the inset in Fig. 15(a). The LO branch is then the dominant branch limiting the transport properties, as the mobility is mostly contributed from electrons in this energy range. For holes of GaAs, the LO phonon scattering is comparable to the scattering from other phonon branches, as shown in Fig. 15(b). For holes below 35 meV, the contribution from LO phonons is only about 40%–60%, and it increases to 80% at 35 meV when the LO emission processes start to occur, as shown in the inset in Fig. 15(b).

Although the ERTA underestimates the mobility, the mode-specific analysis based on the ERTA can still apply to the transport properties qualitatively. The iterative solution gives a larger mobility than the ERTA, indicating that the total scattering for the transport is actually weaker. The weakened scattering comes from LO phonons, since the divergent electron-phonon coupling elements of LO phonons cause strongly anisotropic scattering [13,51]. Considering that LO phonons contribute more than 80% to the electron scattering for energy, they still dominate the scattering for transport. For holes, LO phonons contribute 40%– 80% to the scattering for energy. Their contribution to the scattering for transport is reduced and thus the other phonon branches have an increased influence on the mobility. Therefore, the analysis of different scattering terms remains valid qualitatively for the mobility. Note that the scattering rate for energy itself is also very important, since it is directly related to the linewidth, a quantity relevant to the equilibrium state.

IV. CONCLUSIONS

In summary, the electron and hole mobilities of Si and GaAs are studied by combining the Wannier function interpolation of the electron-phonon coupling matrix obtained from first-principles calculations and the Boltzmann transport equation. The momentum relaxation time approximation has an improved accuracy compared to the energy relaxation time approximation, especially in GaAs. The calculated mobilities are in reasonable agreement with the experiments. In Si and GaAs, the spin-orbit coupling effect significantly affects the hole mobilities but has no effect on electrons. For electrons of GaAs, the calculated mobilities depend on the band structure characterized by the electron effective mass and Γ-L energy gap, which is the major cause of the discrepancies in the literature. In GaAs, at room temperature, the largest hole mean free path is 45 nm, much smaller than that for electrons, namely, 165 nm. The longitudinal optical phonons dominate the electron scattering process in GaAs, however, the other phonon branches also make a comparable contribution to the hole scattering.

ACKNOWLEDGMENTS

We thank Dr. J.-J. Zhou and Dr. T.-H. Liu for helpful discussions on the calculation of GaAs. We acknowledge support from the Natural Science Foundation of China under Grant No. 11704258, the Natural Science Foundation of Guangdong Province under Grant No. 2017A030310377, and the Natural Science Foundation of Shenzhen City under Grant No. JCYJ20170412105922384. J.M. also acknowledge support from the China Postdoctoral Science Foundation under Grant No. 2017M612707.

[1] W. Li, J. Carrete, N. A. Katcho, and N. Mingo, Comput. Phys. Commun. **185**, 1747 (2014).

[2] A. Togo, L. Chaput, and I. Tanaka, Phys. Rev. B **91**, 094306 (2015).

[3] T. Tadano, Y. Gohda, and S. Tsuneyuki, J. Phys.: Condens. Matter **26**, 225402 (2014).
[4] F. Giustino, Rev. Mod. Phys. **89**, 015003 (2017).
[5] J. Noffsinger, F. Giustino, B. D. Malone, C.-H. Park, S. G. Louie, and M. L. Cohen, Comput. Phys. Commun. **181**, 2140 (2010).
[6] S. Poncé, E. Margine, C. Verdi, and F. Giustino, Comput. Phys. Commun. **209**, 116 (2016).
[7] C. Verdi and F. Giustino, Phys. Rev. Lett. **115**, 176401 (2015).
[8] B. Qiu, Z. Tian, A. Vallabhaneni, B. Liao, J. M. Mendoza, O. D. Restrepo, X. Ruan, and G. Chen, Europhys. Lett. **109**, 57006 (2015).
[9] B. Liao, J. Zhou, B. Qiu, M. S. Dresselhaus, and G. Chen, Phys. Rev. B **91**, 235419 (2015).
[10] H. Fröhlich, Adv. Phys. **3**, 325 (1954).
[11] B. Himmetoglu, A. Janotti, H. Peelaers, A. Alkauskas, and C. G. Van de Walle, Phys. Rev. B **90**, 241204 (2014).
[12] J. Sjakste, N. Vast, M. Calandra, and F. Mauri, Phys. Rev. B **92**, 054307 (2015).
[13] W. Li, Phys. Rev. B **92**, 075405 (2015).
[14] J.-J. Zhou and M. Bernardi, Phys. Rev. B **94**, 201201(R) (2016).
[15] T.-H. Liu, J. Zhou, B. Liao, D. J. Singh, and G. Chen, Phys. Rev. B **95**, 075206 (2017).
[16] M. Omini and A. Sparavigna, Physica B (Amsterdam) **212**, 101 (1995).
[17] L. Lindsay, D. Broido, and T. Reinecke, Phys. Rev. B **87**, 165201 (2013).
[18] P. Giannozzi, S. Baroni, N. Bonini, M. Calandra, R. Car, C. Cavazzoni, D. Ceresoli, G. L. Chiarotti, M. Cococcioni, I. Dabo, A. D. Corso, S. de Gironcoli, S. Fabris, G. Fratesi, R. Gebauer, U. Gerstmann, C. Gougoussis, A. Kokalj, M. Lazzeri, L. Martin-Samos, N. Marzari, F. Mauri, R. Mazzarello, S. Paolini, A. Pasquarello, L. Paulatto, C. Sbraccia, S. Scandolo, G. Sclauzero, A. P. Seitsonen, A. Smogunov, P. Umari, and R. M. Wentzcovitch, J. Phys.: Condens. Matter **21**, 395502 (2009).
[19] A. D. Corso, Comput. Mater. Sci. **95**, 337 (2014).
[20] J. P. Perdew and A. Zunger, Phys. Rev. B **23**, 5048 (1981).
[21] M. E. Straumanis and E. Z. Aka, J. Appl. Phys. **23**, 330 (1952).
[22] A. W. Stevenson, Acta Crystallogr. Sec. A **50**, 621 (1994).
[23] B. D. Malone and M. L. Cohen, J. Phys.: Condens. Matter **25**, 105503 (2013).
[24] G. Harbeke, O. Madelung, and U. Rössler, in *Numerical Data and Functional Relationships in Science and Technology*, edited by O. Magelung (Springer-Verlag, Berlin, 1982).
[25] M. Rohlfing, P. Krüger, and J. Pollmann, Phys. Rev. B **48**, 17791 (1993).
[26] R. N. Dexter, B. Lax, A. F. Kip, and G. Dresselhaus, Phys. Rev. **96**, 222 (1954).
[27] L. E. Ramos, L. K. Teles, L. M. R. Scolfaro, J. L. P. Castineira, A. L. Rosa, and J. R. Leite, Phys. Rev. B **63**, 165210 (2001).
[28] D. Yu, Y. Zhang, and F. Liu, Phys. Rev. B **78**, 245204 (2008).
[29] S. Wei and M. Y. Chou, Phys. Rev. B **50**, 2221 (1994).
[30] F. J. Morin, T. H. Geballe, and C. Herring, Phys. Rev. **105**, 525 (1957).
[31] R. A. Logan and A. J. Peters, J. Appl. Phys. **31**, 122 (1960).
[32] P. Norton, T. Braggins, and H. Levinstein, Phys. Rev. B **8**, 5632 (1973).
[33] C. Canali, C. Jacoboni, F. Nava, G. Ottaviani, and A. Alberigi-Quaranta, Phys. Rev. B **12**, 2265 (1975).
[34] M. Fiorentini and N. Bonini, Phys. Rev. B **94**, 085204 (2016).
[35] F. J. Morin and J. P. Maita, Phys. Rev. **96**, 28 (1954).
[36] G. Ottaviani, L. Reggiani, C. Canali, F. Nava, and A. Alberigi-Quaranta, Phys. Rev. B **12**, 3318 (1975).
[37] J. Zhou, B. Liao, B. Qiu, S. Huberman, K. Esfarjani, M. S. Dresselhaus, and G. Chen, Proc. Natl. Acad. Sci. USA **112**, 14777 (2015).
[38] M. Bernardi, D. Vigil-Fowler, J. Lischner, J. B. Neaton, and S. G. Louie, Phys. Rev. Lett. **112**, 257402 (2014).
[39] M. Bernardi, Eur. Phys. J. B **89**, 239 (2016).
[40] D. Lock, K. R. Rusimova, T. L. Pan, R. E. Palmer, and P. A. Sloan, Nat. Commun. **6**, 8365 (2015).
[41] K. Esfarjani, G. Chen, and H. T. Stokes, Phys. Rev. B **84**, 085204 (2011).
[42] A. I. Boukai, Y. Bunimovich, J. Tahir-Kheli, J.-K. Yu, W. A. Goddard III, and J. R. Heath, Nature **451**, 168 (2008).
[43] A. I. Hochbaum, R. Chen, R. D. Delgado, W. Liang, E. C. Garnett, M. Najarian, A. Majumdar, and P. Yang, Nature **451**, 163 (2008).
[44] E. K. Lee, L. Yin, Y. Lee, J. W. Lee, S. J. Lee, J. Lee, S. N. Cha, D. Whang, G. S. Hwang, K. Hippalgaonkar, A. Majumdar, C. Yu, B. L. Choi, J. M. Kim, and K. Kim, Nano Lett. **12**, 2918 (2012).
[45] M. Gmitra and J. Fabian, Phys. Rev. B **94**, 165202 (2016).
[46] L. W. Molenkamp, R. Eppenga, G. W. 't Hooft, P. Dawson, C. T. Foxon, and K. J. Moore, Phys. Rev. B **38**, 4314 (1988).
[47] A. K. Walton and U. K. Mishra, J. Phys. C **1**, 533 (1968).
[48] C. S. Wang and B. M. Klein, Phys. Rev. B **24**, 3393 (1981).
[49] Y.-S. Kim, M. Marsman, G. Kresse, F. Tran, and P. Blaha, Phys. Rev. B **82**, 205212 (2010).
[50] D. Strauch and B. Dorner, J. Phys.: Condens. Matter **2**, 1457 (1990).
[51] M. Lundstrom, *Fundametals of Carrier Transport* (University Press, Cambridge, UK, 2000), pp. 139–141.
[52] H. Hicks and D. Manley, Solid State Commun. **7**, 1463 (1969).
[53] D. L. Rode, Phys. Rev. B **2**, 1012 (1970).
[54] G. Stillman, C. Wolfe, and J. Dimmock, J. Phys. Chem. Solids **31**, 1199 (1970).
[55] K. Nichols, C. M. Yee, and C. Wolfe, Solid State Electron. **23**, 109 (1980).
[56] D. E. Hill, J. Appl. Phys. **41**, 1815 (1970).
[57] A. L. Mears and R. A. Stradling, J. Phys. C **4**, L22 (1971).
[58] J. S. Blakemore, J. Appl. Phys. **53**, R123 (1982).
[59] M. H. Kim, S. S. Bose, B. J. Skromme, B. Lee, and G. E. Stillman, J. Electron. Mater. **20**, 671 (1991).
[60] A. F. J. Levi, J. R. Hayes, P. M. Platzman, and W. Wiegmann, Phys. Rev. Lett. **55**, 2071 (1985).
[61] M. Heiblum, D. Galbi, and M. Weckwerth, Phys. Rev. Lett. **62**, 1057 (1989).